

Temporal Spinwave Fabry-Pérot Interferometry via Coherent Population Trapping

Ruihuan Fang,^{1,2} Chengyin Han,¹ Xunda Jiang,^{1,2} Yuxiang Qiu,^{1,2} Yuanyuan Guo,^{1,2} Minhua Zhao,^{1,2} Jiahao Huang,^{1,*} Bo Lu,^{1,†} and Chaohong Lee^{1,2,‡}

¹*Guangdong Provincial Key Laboratory of Quantum Metrology and Sensing & School of Physics and Astronomy, Sun Yat-Sen University (Zhuhai Campus), Zhuhai 519082, China*

²*State Key Laboratory of Optoelectronic Materials and Technologies, Sun Yat-Sen University (Guangzhou Campus), Guangzhou 510275, China*

(Dated: December 22, 2024)

Ramsey spectroscopy via coherent population trapping (CPT) is essential in precision measurements. The conventional CPT-Ramsey fringes contain numbers of almost identical oscillations and so that it is difficult to identify the central fringe. Here, we experimentally demonstrate a temporal spinwave Fabry-Pérot interferometry via double- Λ CPT of laser-cooled ^{87}Rb atoms. Due to the constructive interference of temporal spinwaves, the transmission spectrum appears as a comb of equidistant peaks in frequency domain and thus the central Ramsey fringe can be easily identified. From the optical Bloch equations for our five-level double- Λ system, the transmission spectrum is analytically explained by the Fabry-Pérot interferometry of temporal spinwaves. Due to small amplitude difference between the two Landé factors, each peak splits into two when the external magnetic field is not too weak. This “unexpected” peak splitting can be employed to measure an unknown magnetic field without involving magneto-sensitive transitions.

Coherent population trapping (CPT) [1], a result of destructive quantum interference between different transition paths, is of great importance in quantum science and technology. CPT spectroscopy has been extensively employed in quantum engineering and quantum metrology, such as, all-optical manipulation [2–7], atomic cooling [8], atomic clocks [9–12], and atomic magnetometers [13–16]. To narrow the CPT resonance linewidth, one may implement Ramsey interferometry in which two CPT pulses are separated by an integration time of the dark state for a time duration T [10, 17, 18]. In a CPT-Ramsey interferometry, the fringe-width $\Delta\nu=1/(2T)$ is independent of the CPT laser intensity and so that one may narrow the linewidth via increasing the time duration T [10, 18]. However, it becomes difficult to identify the central CPT-Ramsey fringe from adjacent ones, since the adjacent-fringe amplitudes are almost equal to the central-fringe amplitude [19, 20]. Thus it becomes very important to suppress the non-central fringes.

In order to suppress the non-central fringes, a widely used and highly efficient way is inserting a CPT pulse sequence between the two CPT-Ramsey pulses. By employing the techniques of multi-pulse phase-stepping [21, 22] or repeated query [20], the non-central fringes have been successfully suppressed. Similarly, high-contrast transparency comb [23] has been achieved via electromagnetically-induced-transparency multi-pulse interference [24]. The existed experiments of multi-pulse CPT interference are almost performed under the σ - σ configuration, in which the two-photon transition occurs between states of the same magnetic quantum number. However, under the σ - σ configuration, atoms will gradually accumulate in a “trap” state that does not contribute ground-state coherence [25]. To eliminate undesired atomic accumulations with no con-

tributions to ground-state coherence, one may employ the lin||lin configuration [26–29]. Under the lin||lin configuration, a five-level double- Λ system is constructed by simultaneously coupling two sets of ground states to a common excited state. Up to now, the multi-pulse CPT interference has never been demonstrated in experiments under the lin||lin configuration.

Moreover, by employing multi-beam interference, the optical Fabry-Pérot (FP) interferometer has been widely used as a bandpass filter that transmits light of certain frequencies [30, 31]. In analogy to multi-beam interference in spatial domain, multi-pulse interference in temporal domain has been proposed for two-level systems [32] and three-level Λ systems [24, 33]. The multi-pulse interferences, such as Carr-Purcell decoupling [34] and periodic dynamical decoupling [35], have enabled versatile applications in quantum sensing [36] from narrower spectral response, sideband suppression, to environmental noise filtering. To the best of our knowledge, it is the first time that we demonstrate the temporal spinwave FP interferometry via multi-pulse CPT-Ramsey interference in a double- Λ system.

In this Letter, based upon the double- Λ CPT in an ensemble of laser-cooled ^{87}Rb atoms under the lin||lin configuration, we experimentally demonstrate the temporal spinwave FP interferometry. The interferometry is carried out with the multi-pulse CPT-Ramsey interference. Due to the temporal spinwave interference, the transmission spectrum appears as a comb with multiple equidistant interference peaks and the central CPT-Ramsey fringe can be easily identified. The distance between adjacent peaks is exactly the repeated frequency of the applied CPT pulses, analogous to the free spectral range (FSR) of an optical cavity. Accordingly, side fringes between two interference peaks are suppressed by

destructive interference. Based upon the optical Bloch equations for the five-level double- Λ system, we develop an analytical theory for the temporal spinwave FP interferometry and well explain the transmission spectrum in experiments.

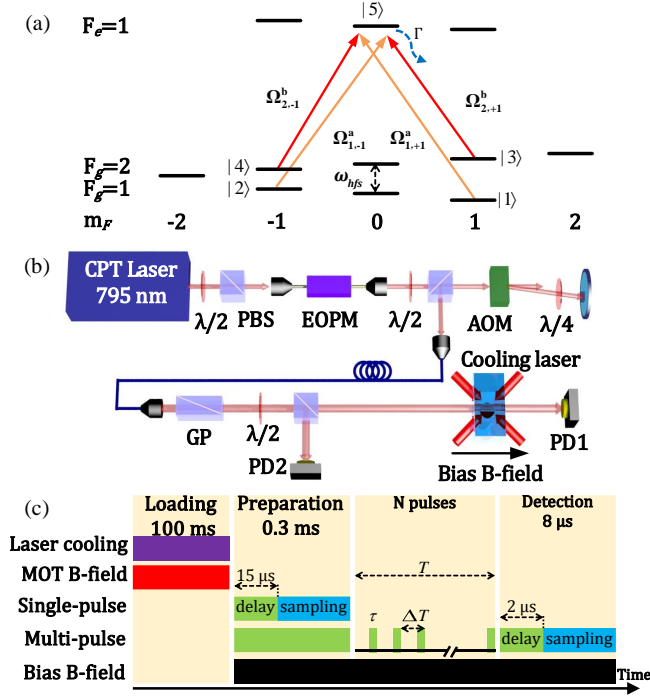


FIG. 1: (Color online) Experimental schematic. (a) Energy levels for double- Λ CPT of ^{87}Rb under the lin||lin configuration. The symbols are detailedly defined in the main texts. (b) The schematic diagram of the experimental apparatus. PBS: polarization beam splitter, EOPM: electro-optic phase modulator, PD: photodetector, AOM: acousto-optic modulator, GP: Glan prism. (c) Experimental timing sequence. A periodic CPT pulse sequence with pulse length τ and pulse period ΔT is inserted between two CPT-Ramsey pulses respectively called as preparation and detection.

The experimental schematic is shown in Fig. 1. Under the lin||lin configuration, two CPT fields are linearly polarized to the same direction orthogonal to the applied magnetic field. We choose the double- Λ system constructed by the D1 line of ^{87}Rb , see Fig. 1(a). A bichromatic field with frequencies of ω_a and ω_b simultaneously couples two sets of ground states $\{|1\rangle = |F_g=1, m_F=+1\rangle, |2\rangle = |F_g=1, m_F=-1\rangle\}$ and $\{|3\rangle = |F_g=2, m_F=+1\rangle, |4\rangle = |F_g=2, m_F=-1\rangle\}$ to the common excited state $|5\rangle = |F_e=1, m_F=0\rangle$. The eigenfrequencies for five involved levels are respectively $\omega_{1, \pm 1}$, $\omega_{2, \pm 1}$ and ω_e . The two-photon detuning is $\delta = (\omega_a - \omega_b) - \omega_{hfs}$. Γ is the excited-state decay rate. The Rabi frequencies for transitions from four ground states to the common excited state are respectively denoted by $\Omega_{1, \pm 1}^a$ and $\Omega_{2, \pm 1}^b$.

We perform the temporal spinwave FP interferometry

with laser-cooled atoms released from a magneto-optical trap (MOT). The schematic diagram of our experimental apparatus is shown in Fig. 1(b). Within an ultra-high vacuum cell with the pressure of 10^{-8} Pa, the ^{87}Rb atoms are cooled and trapped via a three-dimensional MOT which is created by laser beams and a quadruple magnetic field produced by a pair of magnetic coils. Two external cavity diode lasers (ECDL) are used as the cooling and repumping lasers that are locked to the D2 cycling transition with a saturated absorption spectrum (SAS). In order to eliminate the stray magnetic field, three pairs of Helmholtz coils are used to cancel ambient magnetic fields. In addition, a pair of Helmholtz coil is used to apply a bias magnetic field aligned with the propagation direction of CPT laser beam to split the Zeeman sublevels.

The CPT laser source is provided by an ECDL locked to the $|F_g=2\rangle \rightarrow |F_e=1\rangle$ transition of ^{87}Rb D1 line at 795 nm. The CPT beam is generated by modulating a single laser with a fiber-coupled electro-optic phase modulator (EOPM). The positive first-order sideband forms the Λ systems with the carrier. The 6.835-GHz modulated frequency matches the two hyperfine ground state. We set the powers of the first-order sidebands equal to the carrier signal by monitoring their intensities with a FP cavity. Following the EOPM, an acousto-optic modulator (AOM) is used to generate the CPT pulse sequence. The modulated laser beams are coupled into a polarization maintaining fiber and collimated to an 8-mm-diameter beam after the fiber. A Glan prism is used to purify the polarization. Then the CPT beam is equally separated into two beams by a half-wave plate and a polarization beam splitter (PBS). One beam is detected by the photodetector [PD2 in Fig. 1(b)] as a normalization signal S_N to reduce the effect of intensity noise on the CPT signals. The other beam is sent to interrogate the cold atoms and collected on the CPT photodetector as S_T [PD1 in Fig. 1(b)]. The transition signal (TS) are given by $S_{TS} = S_T / S_N$.

The experimental timing sequence is shown in Fig. 1(c). Before implementing the CPT-Ramsey interferometry, about 10^7 ^{87}Rb atoms are cooled and trapped within a 100-ms cooling period. Then the atoms are interrogated under free fall after turning off the MOT magnetic field and the cooling laser beams. In order to make sure that the MOT magnetic field decays to zero, the CPT beams accompanied with a bias magnetic field are applied after 1 ms waiting time. The first CPT-Ramsey pulse with a duration of 0.3 ms is used to pump the atoms into the dark state and here called as preparation. If no following pulses are applied, through averaging the collected voltage signals of this pulse after a delay of 15 μs , the single-pulse CPT spectrum is obtained by scanning the modulation frequency of EOPM, see Fig. 2(a). By fitting the spectrum with a Lorentz shape, its full width at half maximum (FWHM) is given as 27

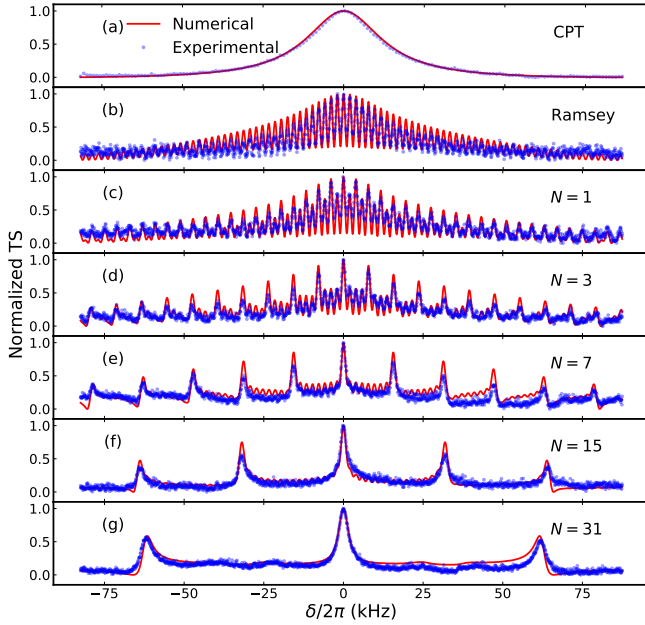


FIG. 2: (Color online) Experimental transmission signals (TS) for different schemes. (a) A Lorentz fitting of single-pulse CPT spectrum shows a full width at half maximum (FWHM) is 27 kHz. (b) Two-pulse CPT-Ramsey spectrum is obtained with a integration time of 0.5 ms. (c)-(g) Multi-pulse CPT-Ramsey spectra via temporal spinwave FP interferometry of N equidistant pulses with a length $\tau=2 \mu\text{s}$ into the integration time of 0.5 ms.

kHz. By comparing the numerical spectrum obtained from the optical Bloch equations, the four Rabi frequencies are estimated as $\pm\Omega_{1,+1}^a = \frac{1}{\sqrt{3}}\Omega_{2,\pm 1}^b = \frac{1.25}{2\pi}$ MHz. The CPT-Ramsey spectra are given by sampling the signal voltages during the detection pulse (the second CPT-Ramsey pulse) after a delay of $2 \mu\text{s}$. Without additional CPT pulses between the two CPT-Ramsey pulses, the spectrum gives the conventional CPT-Ramsey spectrum, see Fig. 2(b). Obviously, in such a conventional CPT-Ramsey spectrum, the central fringe cannot be readily distinguished from neighbouring fringes.

The temporal spinwave FP interferometry is performed by inserting a periodic CPT pulse sequence between the two CPT-Ramsey pulses. The minimum length of a single pulse is limited to $1 \mu\text{s}$, given by the precision of the controlled digital I/O given. In Fig. 2(c)-(g), we show the spectra for different pulse numbers N . Given the pulse length $\tau=2 \mu\text{s}$ and the integration time $T = 0.5$ ms, because of the constructive interference, high-contrast transmission peaks gradually appear when the pulse number N increases. The distance between two neighboring peaks is exactly given by the repeated frequency. Due to the destructive interference, the background becomes more flat while the pulse number N increases, which makes the central fringe more distinguishable at a small expense of the linewidth.

We theoretically analyze the aspects of temporal spinwave FP interference using the Bloch equations for a five-level atomic system and obtain an analytical expression for the spectra. Generally, by ignoring the ground states exchange, the time-evolution is governed by a Liouville equation [37, 38]

$$\frac{\partial \rho}{\partial t} = -\frac{i}{\hbar}(\hat{H}\rho - \rho\hat{H}^\dagger) + \dot{\rho}_{\text{trans-decay}} + \dot{\rho}_{\text{src}}, \quad (1)$$

with the density matrix $\rho = \sum_{j=1}^5 \sum_{i=1}^5 \rho_{ij} |i\rangle\langle j|$, the decoherence between ground states $\dot{\rho}_{\text{trans-decay}} = \sum_{j=2}^4 \sum_{i=1}^{j-1} (-\gamma_{ij} \rho_{ij} |i\rangle\langle j| + h.c.)$ with the decoherence rates γ_{ij} , the population decay $\dot{\rho}_{\text{src}} = \sum_{i=1}^4 \frac{\Gamma}{4} \rho_{55} |i\rangle\langle i|$, and the Hamiltonian $\hat{H} = \hbar [(\delta + g_1 \frac{\mu_B}{\hbar} B_z) |1\rangle\langle 1| + (\delta - g_1 \frac{\mu_B}{\hbar} B_z) |2\rangle\langle 2| + g_2 \frac{\mu_B}{\hbar} B_z |3\rangle\langle 3| - g_2 \frac{\mu_B}{\hbar} B_z |4\rangle\langle 4| - \frac{i\Gamma}{2} |5\rangle\langle 5| + \frac{\Omega_1}{2} (|1\rangle\langle 5| + |2\rangle\langle 5| + h.c.) + \frac{\Omega_2}{2} (|3\rangle\langle 5| + |4\rangle\langle 5| + h.c.)]$. Here, B_z is the bias magnetic field along the light propagation direction, μ_B is the Bohr magneton, $\{\Omega_1 = \Omega_{1,+1}^a = -\Omega_{1,-1}^a, \Omega_2 = \Omega_{2,\pm 1}^b\}$ are two Rabi frequencies, and $\{g_1, g_2\}$ are respectively the Landé g factors for ground states $F=\{1, 2\}$. For ^{87}Rb , g_1 and g_2 have a tiny different value but opposite signs, therefore there are two magneto-insensitive transitions: $|1\rangle \rightarrow |4\rangle$ and $|2\rangle \rightarrow |3\rangle$. Experimentally, each density matrix element should be summed over the atoms contributing signals, i.e. $\rho_{ij} = \langle \hat{\rho}_{ij} \rangle$ [39].

The CPT-based spectra are experimentally obtained from the transmission of CPT light. The transmission signal is proportional to $(1 - \rho_{55})$, that is, the absorption is proportional to the excited-state population ρ_{55} . For simplicity, we do not consider degenerate Zeeman sublevels and set all four Rabi frequencies as the average Rabi frequency [40]. To compare with the experimental observation, the average Rabi frequency can be given as $\Omega = \sqrt{(\Omega_1^2 + \Omega_2^2)/2}$ [41]. Due to the large decoherence rates $\{\gamma_{12}, \gamma_{13}, \gamma_{24}, \gamma_{34}\}$ of magneto-sensitive transitions [42], the corresponding density matrix elements $\{\rho_{12}, \rho_{13}, \rho_{24}, \rho_{34}\}$ can be ignored near the magneto-insensitive two-photon resonance. Thus, using the adiabatically eliminating and resonance approximation [43]

$$\rho_{55} = \frac{\Omega^2}{\Gamma^2} + \frac{2\Omega^2}{\Gamma^2} \text{Re}(\rho_{14} + \rho_{23}). \quad (2)$$

Under the lin||lin configuration, for a weakly magnetic field, the two CPT resonances are nearly identical [25, 29] as $(g_1 + g_2) \mu_B B_z \rightarrow 0$. Applying N multiple CPT pulses, we analytically obtain [38]

$$\rho_{55} = \frac{\Omega^2}{\Gamma^2} + \frac{4\Omega^2}{\Gamma^2} \text{Re}[\sigma(\delta)], \quad (3)$$

with

$$\sigma(\delta) = f(\delta) \sum_{l=1}^{N_c} e^{-\frac{\Omega^2}{\Gamma^2} \sum_{k=l+1}^{N_c} \tau(k)} \left[1 - e^{-\left(\frac{\Omega^2}{\Gamma^2} + i\delta\right) \tau(l)} \right] \times e^{-i\delta \sum_{k=l+1}^{N_c} \Delta T(k)}.$$

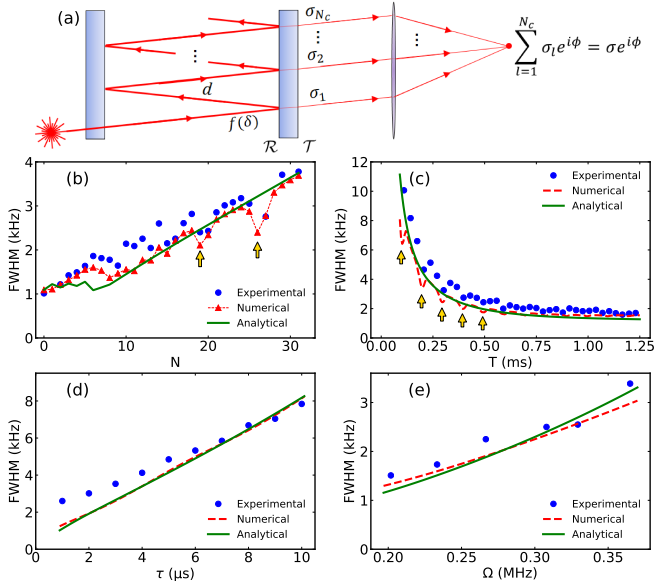


FIG. 3: (Color online) Linewidth aspects of the temporal spin-wave FP interferometry. Where, the bias magnetic field is chosen as $B_z=0.116$ G and the yellow arrows label the exotic dips due to magneto-sensitive transitions. (a) The temporal spinwave FP interferometry is analogous to the light transmission in a FP cavity. Where, \mathcal{R} and \mathcal{T} are respectively the reflection and the transmission coefficients, the cavity length $d = \Delta T c/2$, and the free spectral range (FSR) $\Delta\nu_{FSR}=c/2d=1/\Delta T$. (b) The linewidth versus the pulse number N with $\Omega=\frac{1.77}{2\pi}$ MHz, $T=0.5$ ms and $\tau=2$ μ s. (c) The linewidth versus the integration time T with $\Omega=\frac{1.77}{2\pi}$ MHz, $N=15$ and $\tau=2$ μ s. (d) The linewidth versus the pulse length τ with $\Omega=\frac{1.77}{2\pi}$ MHz, $N=15$ and $\Delta T=0.031$ ms. (e) The linewidth versus the average Rabi frequency Ω with $\tau=2$ μ s, $N=15$ and $\Delta T=0.031$ ms.

Here, $\tau(l)$ and $\Delta T(l)$ are respectively the length and the interval for the l -th CPT pulse, $f(\delta) = -\frac{\Omega^2}{4\Gamma(i\delta + \frac{\Omega^2}{T})}$, and $N_c = N + 2$ is the total number of CPT pulses including the preparation and detection pulses. To consistent with our experiment, the pulse length and the pulse interval are chosen as $\tau(l)=\tau$ and $\Delta T(l)=\Delta T$, respectively. Therefore $\sigma(\delta)$ can be simplified as

$$\sigma(\delta) = \sum_{l=1}^{N_c} \sigma_l(\delta), \quad (4)$$

with $\sigma_l(\delta)=f(\delta)\mathcal{R}^{(l-1)}\mathcal{T}e^{-i(l-1)\delta\Delta T}$, the reflection coefficient $\mathcal{R} \equiv e^{-\frac{\Omega^2}{T}\tau}$, and the transmission coefficient $\mathcal{T} \equiv 1 - e^{-\left(\frac{\Omega^2}{T}+i\delta\right)\tau}$. Obviously, Eq. (4) is analogous to the light transmission in a FP cavity, see Fig. 3(a). According to Eq. (4), constructive interferences occur at $\delta\Delta T=2m\pi$ ($m \in \mathbb{Z}$), which exactly give the resonance peaks in our experimental spectra (see Fig. 2).

To further show the power of our analytical results, we compare the experimental, numerical and

analytical linewidths. In analogy to the linewidth of FP cavity, the FWHM of spectrum [44] can be given as $\Delta\nu=(2\Delta\nu_{FSR}/\pi)\arcsin\left[(1-\sqrt{\mathcal{R}})/(2\sqrt[4]{\mathcal{R}})\right]$ with $\Delta\nu_{FSR}=1/\Delta T$ corresponding to the FSR of FP cavity. Accordingly, the linewidth will increase with the FSR which is proportional to the repeated frequency of inserted CPT pulses. Fig. 3 clearly shows that the experimental results are well consistent with the analytical and numerical ones. The linewidth increases with the pulse number N for a given integration time T , while it will decrease with the integration time T for a given pulse number N . However, as labelled by the yellow arrows in Fig. 3 (b,c), there appear some exotic dips in the experimental and numerical results. These exotic dips are actually caused by a tiny contribution of magneto-sensitive transitions under the resonant condition $m/(B_z\Delta T) = 1.4$ MHz/G, see more details in Supplementary Information. The linewidth increases with the pulse length τ and the average Rabi frequency Ω when the other parameters are fixed, see Fig. 3 (d,e). Here, the Rabi frequency is experimentally obtained by fitting CPT line shape with $f(\delta)$. As the reflection coefficient $\mathcal{R}=e^{-\frac{\Omega^2}{T}\tau}$, this indicates that the linewidth decreases with the reflection coefficient.

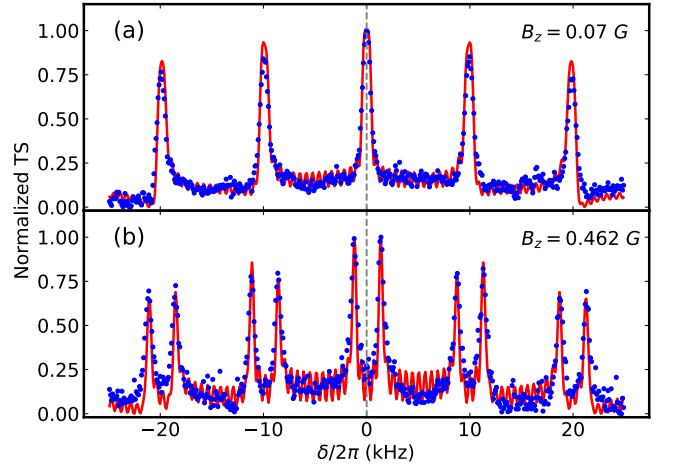


FIG. 4: (Color online) Experimental TS (blue dots) under different bias magnetic fields B_z . In the experiments, 15 CPT pulses with length $\tau = 2$ μ s are applied during the integration time $T = 1.6$ ms. The numerical results (red lines) is fitted with $\Omega = \frac{1.6}{2\pi}$ MHz. The vertical gray dash line labels $\delta = 0$. (a) $B_z = 0.07$ G. (b) $B_z = 0.462$ G.

In above, due to the bias magnetic field is very weak, the two magnetic-insensitive transitions $|1\rangle \rightarrow |4\rangle$ and $|2\rangle \rightarrow |3\rangle$ show no difference. Actually, the two involved Landé g factors $g_1 = -0.5017$ and $g_2 = 0.4997$ have small amplitude difference and this difference will bring a frequency shift $2|g_1 + g_2|\frac{\mu_B}{h}B_z = 5568B_z$ Hz/G between the two magnetic-insensitive transitions. Thus, as shown in Fig. 4, each peak splits into two when the bias mag-

netic field increases to a strength such that the frequency shift is larger than the linewidth [38]. This “unexpected” peak splitting is beneficial for not only eliminating linear Zeeman shifts by averaging each pair of peaks, but also measuring a magnetic field without involving magneto-sensitive transitions.

In conclusion, we have experimentally demonstrated a temporal spinwave FP interferometry via laser-cooled ^{87}Rb atoms under the lin||lin configuration. The transmission spectrum appears as a high-contrast comb, in which a sequence of equidistant resonant peaks and non-resonant plains are respectively due to constructive and destructive interferences. We develop an analytical theory for the temporal spinwave FP interferometry based upon the optical Bloch equations for our five-level double- Λ CPT system. Beyond identifying the central CPT-Ramsey fringe, our scheme could be directly used to measure clock transition frequency [9–12] and static magnetic field [13–16]. The temporal spinwave FP interferometry protocol could be also extended to other systems, such as, coherent storage of photons in EIT [45] and coherent control of internal spin states in diamond defects [6] or artificial atoms [46–48].

Acknowledgements

R. Fang, C. Han and X. Jiang contributed equally to this work. This work is supported by the Key-Area Research and Development Program of Guangdong Province under Grants No. 2019B030330001, the National Natural Science Foundation of China (NNSFC) under Grants No. 11874434 and No. 11574405, and the Science and Technology Program of Guangzhou (China) under Grants No. 201904020024. C. H. is supported by the Fundamental Research Funds for Central Universities under Grant No. 19lgpy275. B. L. is supported by the Guangdong Natural Science Foundation under Grants No. 2018A030313988, the Guangzhou Science and Technology Projects under Grants No. 201804010497, and the Fundamental Research Funds for Central Universities under Grants No. 19lgpy283.

* Electronic address: hjiahao@mail2.sysu.edu.cn

† Electronic address: lubo3@mail.sysu.edu.cn

‡ Electronic address: lichao2@mail.sysu.edu.cn

- [1] H. R. Gray, R. M. Whitley, and C. R. Stroud, *Opt. Lett.* **3**, 218 (1978).
- [2] L. J. Rogers, K. D. Jahnke, M. H. Metsch, A. Sipahigil, J. M. Binder, T. Teraji, H. Sumiya, J. Isoya, M. D. Lukin, P. Hemmer, and F. Jelezko, *Phys. Rev. Lett.* **113**, 263602 (2014).
- [3] S. Das, P. Liu, B. Grémaud, and M. Mukherjee, *Phys. Rev. A* **97**, 033838 (2018).
- [4] K. Xia, R. Kolesov, Y. Wang, P. Siyushev, R. Reuter, T. Kornher, N. Kukharchyk, A. D. Wieck, B. Villa, S. Yang, and J. Wrachtrup, *Phys. Rev. Lett.* **115**, 093602 (2015).
- [5] C. Santori, P. Tamarat, P. Neumann, J. Wrachtrup, D. Fattal, R. G. Beausoleil, J. Rabreau, P. Olivero, A. D. Greentree, S. Praver, F. Jelezko, and P. Hemmer, *Phys. Rev. Lett.* **97**, 247401 (2006).
- [6] P. Jamonneau, G. Hétet, A. Dréau, J.-F. Roch, and V. Jacques, *Phys. Rev. Lett.* **116**, 043603 (2016).
- [7] K.-K. Ni, S. Ospelkaus, M. H. G. de Miranda, A. Pe’er, B. Neyenhuis, J. J. Zirbel, S. Kotochigova, P. S. Julienne, D. S. Jin, and J. Ye, *Science* **322**, 231 (2008).
- [8] A. Aspect, E. Arimondo, R. Kaiser, N. Vansteenkiste, and C. Cohen-Tannoudji, *Phys. Rev. Lett.* **61**, 826 (1988).
- [9] J. Vanier, *Appl. Phys. B* **81**, 421 (2005).
- [10] M. Merimaa, T. Lindvall, I. Tittonen, and E. Ikonen, *J. Opt. Soc. Am. B* **20**, 273 (2003).
- [11] P. Yun, F. Tricot, C. E. Calosso, S. Micalizio, B. François, R. Boudot, S. Guérandel, and E. de Clercq, *Phys. Rev. Applied* **7**, 014018 (2017).
- [12] X. Liu, E. Ivanov, V. I. Yudin, J. Kitching, and E. A. Donley, *Phys. Rev. Applied* **8**, 054001 (2017).
- [13] M. O. Scully and M. Fleischhauer, *Phys. Rev. Lett.* **69**, 1360 (1992).
- [14] A. Nagel, L. Graf, A. Naumov, E. Mariotti, V. Biancalana, D. Meschede, and R. Wynands, *Europhys. Lett.* **44**, 31 (1998).
- [15] P. D. D. Schwindt, S. Knappe, V. Shah, L. Hollberg, J. Kitching, L.-A. Liew, and J. Moreland, *Appl. Phys. Lett.* **85**, 6409 (2004).
- [16] R. Tripathi and G. S. Pati, *IEEE Photonics Journal* **11**, 1 (2019).
- [17] T. Zanon, S. Guérandel, E. de Clercq, D. Holleville, N. Dimarcq, and A. Clairon, *Phys. Rev. Lett.* **94**, 193002 (2005).
- [18] J. Vanier, M. W. Levine, D. Janssen, and M. Delaney, *Phys. Rev. A* **67**, 065801 (2003).
- [19] X. Liu, V. I. Yudin, A. V. Taichenachev, J. Kitching, and E. A. Donley, *Appl. Phys. Lett.* **111**, 224102 (2017).
- [20] Z. Warren, M. S. Shahriar, R. Tripathi, and G. S. Pati, *J. Appl. Phys.* **123**, 053101 (2018).
- [21] S. Guérandel, T. Zanon, N. Castagna, F. Dahes, E. de Clercq, N. Dimarcq, and A. Clairon, *IEEE Trans. Instrum. Meas.* **56**, 383 (2007).
- [22] P. Yun, Y. Zhang, G. Liu, W. Deng, L. You, and S. Gu, *Europhys. Lett.* **97**, 63004 (2012).
- [23] S.-J. Yang, J. Rui, H.-N. Dai, X.-M. Jin, S. Chen, and J.-W. Pan, *Phys. Rev. A* **98**, 033802 (2018).
- [24] L. Nicolas, T. Delord, P. Jamonneau, R. Coto, J. Maze, V. Jacques, and G. Hétet, *New J. Phys.* **20**, 033007 (2018).
- [25] A. V. Taichenachev, V. I. Yudin, V. L. Velichansky, and S. A. Zibrov, *Jetp Lett.* **82**, 398 (2005).
- [26] E. Breschi, G. Kazakov, R. Lammegger, G. Miletì, B. Matsov, and L. Windholz, *Phys. Rev. A* **79**, 063837 (2009).
- [27] S. A. Zibrov, I. Novikova, D. F. Phillips, R. L. Walsworth, A. S. Zibrov, V. L. Velichansky, A. V. Taichenachev, and V. I. Yudin, *Phys. Rev. A* **81**, 013833 (2010).
- [28] E. E. Mikhailov, T. Horrom, N. Belcher, and I. Novikova, *J. Opt. Soc. Am. B* **27**, 417 (2010).
- [29] F.-X. Esnault, E. Blanshan, E. N. Ivanov, R. E. Scholten, J. Kitching, and E. A. Donley, *Phys. Rev. A* **88**, 042120 (2013).

- [30] N. Ismail, C. C. Kores, D. Geskus, and M. Pollnau, *Opt. Express* **24**, 16366 (2016).
- [31] J. Poirson, F. Bretenaker, M. Vallet, and A. L. Floch, *J. Opt. Soc. Am. B* **14**, 2811 (1997).
- [32] E. Akkermans and G. V. Dunne, *Phys. Rev. Lett.* **108**, 030401 (2012).
- [33] O. Pinel, J. L. Everett, M. Hosseini, G. T. Campbell, B. C. Buchler, and P. K. Lam, *Sci. Rep.* **5**, 17633 (2015).
- [34] H. Y. Carr and E. M. Purcell, *Phys. Rev.* **94**, 630 (1954).
- [35] L. Viola and S. Lloyd, *Phys. Rev. A* **58**, 2733 (1998).
- [36] C. L. Degen, F. Reinhard, and P. Cappellaro, *Rev. Mod. Phys.* **89**, 035002 (2017).
- [37] M. Shahriar, Y. Wang, S. Krishnamurthy, Y. Tu, G. Pati, and S. Tseng, *J. Mod. Opt.* **61**, 351 (2014).
- [38] In the Supplementary Material, we present more details about: (i) the physical system and its model, (ii) analytical results for the temporal spinwave Fabry-Perot interferometry, and (iii) comparison among numerical, analytical and experimental results.
- [39] A. V. Gorshkov, A. André, M. Fleischhauer, A. S. Sørensen, and M. D. Lukin, *Phys. Rev. Lett.* **98**, 123601 (2007).
- [40] Y.-C. Chen, C.-W. Lin, and I. A. Yu, *Phys. Rev. A* **61**, 053805 (2000).
- [41] P. R. Hemmer, M. S. Shahriar, V. D. Natoli, and S. Ezekiel, *J. Opt. Soc. Am. B* **6**, 1519 (1989).
- [42] I. Baumgart, J.-M. Cai, A. Retzker, M. Plenio, and C. Wunderlich, *Phys. Rev. Lett.* **116**, 240801 (2016).
- [43] D. S. Chuchelov, E. A. Tsygankov, S. A. Zibrov, M. I. Vaskovskaya, V. V. Vassiliev, A. S. Zibrov, V. I. Yudin, A. V. Taichenachev, and V. L. Velichansky, *J. Appl. Phys.* **126**, 054503 (2019).
- [44] A. Siegman, *Lasers* (University Science Books, 1986).
- [45] M. Fleischhauer, A. Imamoglu, and J. P. Marangos, *Rev. Mod. Phys.* **77**, 633 (2005).
- [46] R. Sánchez, C. López-Monís, and G. Platero, *Phys. Rev. B* **77**, 165312 (2008).
- [47] A. Donarini, M. Niklas, M. Schaffberger, N. Paradiso, C. Strunk, and M. Grifoni, *Nat. Commun.* **10**, 381 (2019).
- [48] W. R. Kelly, Z. Dutton, J. Schlafer, B. Mookerji, T. A. Ohki, J. S. Kline, and D. P. Pappas, *Phys. Rev. Lett.* **104**, 163601 (2010).

Supplementary Material

Double- Λ system

The double- Λ system of laser-cooled ^{87}Rb atoms can be described by a five-level model. We label the five levels as (see Fig. S1):

$$\begin{aligned}
 |1\rangle &= |F=1, m_F=+1\rangle, \\
 |2\rangle &= |F=1, m_F=-1\rangle, \\
 |3\rangle &= |F=2, m_F=+1\rangle, \\
 |4\rangle &= |F=2, m_F=-1\rangle, \\
 |5\rangle &= |F'=1, m_F=0\rangle.
 \end{aligned} \tag{S1}$$

The time-evolution of system is governed by the Liouville equation for the density matrix [S1],

$$\frac{\partial}{\partial t} \rho = -\frac{i}{\hbar} (\hat{H} \rho - \rho \hat{H}^\dagger) + \dot{\rho}_{src} + \dot{\rho}_{trans-decay}. \tag{S2}$$

Here, the Hamiltonian \hat{H} reads,

$$\hat{H} = \hbar \begin{pmatrix} \Delta_1 - \frac{i\gamma_g}{2} & 0 & 0 & 0 & \frac{\Omega_{1,+1}^a}{2} \\ 0 & \Delta_2 - \frac{i\gamma_g}{2} & 0 & 0 & \frac{\Omega_{1,-1}^a}{2} \\ 0 & 0 & \Delta_3 - \frac{i\gamma_g}{2} & 0 & \frac{\Omega_{2,+1}^b}{2} \\ 0 & 0 & 0 & \Delta_4 - \frac{i\gamma_g}{2} & \frac{\Omega_{2,-1}^b}{2} \\ \frac{\Omega_{1,+1}^a}{2} & \frac{\Omega_{1,-1}^a}{2} & \frac{\Omega_{2,+1}^b}{2} & \frac{\Omega_{2,-1}^b}{2} & -\frac{i\Gamma}{2} \end{pmatrix}. \tag{S3}$$

In the presence of magnetic field, the diagonal terms of the \hat{H} matrix are defined in terms of the two-photon detuning (δ) and linear Zeeman shift (δ_{Z1} and δ_{Z2}),

$$\begin{aligned}
 \Delta_1 &= \delta + \delta_{Z1}, \\
 \Delta_2 &= \delta - \delta_{Z1}, \\
 \Delta_3 &= \delta_{Z2}, \\
 \Delta_4 &= -\delta_{Z2}.
 \end{aligned} \tag{S4}$$

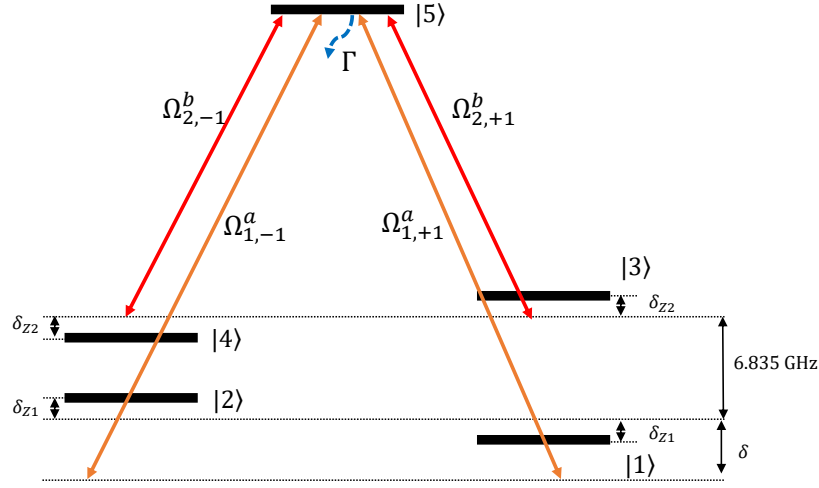


FIG. S5: **Schematic of the five-level model.** The double- Λ configuration of a linearly polarized bichromatic light can be described by a five-level model. In the absence of the external magnetic field, the transition frequencies for $|1\rangle \rightarrow |4\rangle$ and $|2\rangle \rightarrow |3\rangle$ are both 6.835 GHz. When a small magnetic field B_z along z -axis is applied and the second-order Zeeman effect is ignored, these Zeeman sublevels of the hyperfine ground state experience linear Zeeman shift as $\delta_{Z1}=g_1\mu_B B_z/\hbar$ and $\delta_{Z2}=g_2\mu_B B_z/\hbar$, where $g_1=-0.5017$ and $g_2=0.4997$ are Landé g -factors, and $\mu_B=\hbar \cdot 1.4$ MHz/G is the Bohr magneton. Where, $\Omega_{1,\pm 1}^a$ and $\Omega_{2,\pm 1}^b$ are Rabi frequencies.

As shown in Fig. , a bichromatic field with frequencies ω_a and ω_b couples the five levels. Because the laser frequency ω_b is kept resonant to the transition $|F_g=2, m_F=0\rangle \rightarrow |5\rangle$, the two-photon detuning δ is equal to the single-photon detuning δ_1 between laser frequency ω_a and the transition $|F_g=1, m_F=0\rangle \rightarrow |5\rangle$. In Eq. S2, the density matrix is written as

$$\rho = \begin{pmatrix} \rho_{11} & \rho_{12} & \rho_{13} & \rho_{14} & \rho_{15} \\ \rho_{12}^* & \rho_{22} & \rho_{23} & \rho_{24} & \rho_{25} \\ \rho_{13}^* & \rho_{23}^* & \rho_{33} & \rho_{34} & \rho_{35} \\ \rho_{14}^* & \rho_{24}^* & \rho_{34}^* & \rho_{44} & \rho_{45} \\ \rho_{15}^* & \rho_{25}^* & \rho_{35}^* & \rho_{45}^* & \rho_{55} \end{pmatrix}, \quad (\text{S5})$$

and the term $\dot{\rho}_{src}$ reads

$$\dot{\rho}_{src} = \begin{pmatrix} \frac{\Gamma_1}{2}\rho_{55} & 0 & 0 & 0 & 0 \\ 0 & \frac{\Gamma_1}{2}\rho_{55} & 0 & 0 & 0 \\ 0 & 0 & \frac{\Gamma_2}{2}\rho_{55} & 0 & 0 \\ 0 & 0 & 0 & \frac{\Gamma_2}{2}\rho_{55} & 0 \\ 0 & 0 & 0 & 0 & 0 \end{pmatrix} + \begin{pmatrix} \frac{\gamma_g}{3}(\rho_{22} + \rho_{33} + \rho_{44}) & 0 & 0 & 0 & 0 \\ 0 & \frac{\gamma_g}{3}(\rho_{11} + \rho_{33} + \rho_{44}) & 0 & 0 & 0 \\ 0 & 0 & \frac{\gamma_g}{3}(\rho_{11} + \rho_{22} + \rho_{44}) & 0 & 0 \\ 0 & 0 & 0 & \frac{\gamma_g}{3}(\rho_{11} + \rho_{22} + \rho_{33}) & 0 \\ 0 & 0 & 0 & 0 & 0 \end{pmatrix}, \quad (\text{S6})$$

where γ_g is the ground states exchange rate, and $\Gamma_{1,2}$ are the damping rates decaying from the excited states to the ground states $|F=1\rangle$ and $|F=2\rangle$. Generally, one can assume $\Gamma_1 + \Gamma_2 = \Gamma$.

The term $\dot{\rho}_{trans-decay}$ accounts for the decay rate between ground states caused by dephasing and it is in form of

$$\dot{\rho}_{trans-decay} = \begin{pmatrix} 0 & -\gamma_{12}\rho_{12} & -\gamma_{13}\rho_{13} & -\gamma_{14}\rho_{14} & 0 \\ -\gamma_{12}\rho_{12}^* & 0 & -\gamma_{23}\rho_{23} & -\gamma_{24}\rho_{24} & 0 \\ -\gamma_{13}\rho_{13}^* & -\gamma_{23}\rho_{23}^* & 0 & -\gamma_{34}\rho_{34} & 0 \\ -\gamma_{14}\rho_{14}^* & -\gamma_{24}\rho_{24}^* & -\gamma_{34}\rho_{34}^* & 0 & 0 \\ 0 & 0 & 0 & 0 & 0 \end{pmatrix}. \quad (\text{S7})$$

Here, the parameters $\{\gamma_{12}, \gamma_{13}, \gamma_{24}, \gamma_{34}\}$ describe the dephasing of magneto-sensitive transitions and so that they are sensitive to the fluctuations of magnetic field. [S2]. The $\{\gamma_{14}, \gamma_{23}\}$ describe the dephasing of magneto-insensitive transitions and can be regarded as zero.

Analytical Results

From Eq. S2, the optical Bloch equation reads

$$\left\{ \begin{array}{l} \frac{\partial}{\partial t} \rho_{11} = \frac{\Gamma_1}{2} \rho_{55} + \frac{i\Omega_{1,+1}^a}{2} \rho_{15} - \frac{i\Omega_{1,+1}^a}{2} \rho_{15}^* + \frac{\gamma_g}{3} (\rho_{22} + \rho_{33} + \rho_{44}) - i\rho_{11}(\Delta_1 - \frac{i\gamma_g}{2}) + i\rho_{11}(\Delta_1 + \frac{i\gamma_g}{2}), \\ \frac{\partial}{\partial t} \rho_{12} = -\frac{i\Omega_{1,+1}^a}{2} \rho_{25}^* + \frac{i\Omega_{1,-1}^a}{2} \rho_{15} - \gamma_{12} \rho_{12} - i\rho_{12}(\Delta_1 - \frac{i\gamma_g}{2}) + i\rho_{12}(\Delta_2 + \frac{i\gamma_g}{2}), \\ \frac{\partial}{\partial t} \rho_{13} = -\frac{i\Omega_{1,+1}^a}{2} \rho_{35}^* + \frac{i\Omega_{2,+1}^b}{2} \rho_{15} - \gamma_{13} \rho_{13} - i\rho_{13}(\Delta_1 - \frac{i\gamma_g}{2}) + i\rho_{13}(\Delta_3 + \frac{i\gamma_g}{2}), \\ \frac{\partial}{\partial t} \rho_{14} = -\frac{i\Omega_{1,+1}^a}{2} \rho_{45}^* + \frac{i\Omega_{2,-1}^b}{2} \rho_{15} - \gamma_{14} \rho_{14} - i\rho_{14}(\Delta_1 - \frac{i\gamma_g}{2}) + i\rho_{14}(\Delta_4 + \frac{i\gamma_g}{2}), \\ \frac{\partial}{\partial t} \rho_{15} = -\frac{\Gamma}{2} \rho_{15} + \frac{i\Omega_{1,+1}^a}{2} \rho_{11} - \frac{i\Omega_{1,+1}^a}{2} \rho_{55} + \frac{i\Omega_{1,-1}^a}{2} \rho_{12} + \frac{i\Omega_{2,+1}^b}{2} \rho_{13} + \frac{i\Omega_{2,-1}^b}{2} \rho_{14} - i\rho_{15}(\Delta_1 - \frac{i\gamma_g}{2}), \\ \frac{\partial}{\partial t} \rho_{22} = \frac{\Gamma_1}{2} \rho_{55} + \frac{i\Omega_{1,-1}^a}{2} \rho_{25} - \frac{i\Omega_{1,-1}^a}{2} \rho_{25}^* + \frac{\gamma_g}{3} (\rho_{11} + \rho_{33} + \rho_{44}) - i\rho_{22}(\Delta_2 - \frac{i\gamma_g}{2}) + i\rho_{22}(\Delta_2 + \frac{i\gamma_g}{2}), \\ \frac{\partial}{\partial t} \rho_{23} = -\frac{i\Omega_{1,-1}^a}{2} \rho_{35}^* + \frac{i\Omega_{2,+1}^b}{2} \rho_{25} - \gamma_{23} \rho_{23} - i\rho_{23}(\Delta_2 - \frac{i\gamma_g}{2}) + i\rho_{23}(\Delta_3 + \frac{i\gamma_g}{2}), \\ \frac{\partial}{\partial t} \rho_{24} = -\frac{i\Omega_{1,-1}^a}{2} \rho_{45}^* + \frac{i\Omega_{2,-1}^b}{2} \rho_{25} - \gamma_{24} \rho_{24} - i\rho_{24}(\Delta_2 - \frac{i\gamma_g}{2}) + i\rho_{24}(\Delta_4 + \frac{i\gamma_g}{2}), \\ \frac{\partial}{\partial t} \rho_{25} = -\frac{\Gamma}{2} \rho_{25} + \frac{i\Omega_{1,+1}^a}{2} \rho_{12}^* + \frac{i\Omega_{1,-1}^a}{2} \rho_{22} - \frac{i\Omega_{1,-1}^a}{2} \rho_{55} + \frac{i\Omega_{2,+1}^b}{2} \rho_{23} + \frac{i\Omega_{2,-1}^b}{2} \rho_{24} - i\rho_{25}(\Delta_2 - \frac{i\gamma_g}{2}), \\ \frac{\partial}{\partial t} \rho_{33} = \frac{\Gamma_2}{2} \rho_{55} + \frac{i\Omega_{2,+1}^b}{2} \rho_{35} - \frac{i\Omega_{2,+1}^b}{2} \rho_{35}^* + \frac{\gamma_g}{3} (\rho_{11} + \rho_{22} + \rho_{44}) - i\rho_{33}(\Delta_3 - \frac{i\gamma_g}{2}) + i\rho_{33}(\Delta_3 + \frac{i\gamma_g}{2}), \\ \frac{\partial}{\partial t} \rho_{34} = -\frac{i\Omega_{2,+1}^b}{2} \rho_{45}^* + \frac{i\Omega_{2,-1}^b}{2} \rho_{35} - \gamma_{34} \rho_{34} - i\rho_{34}(\Delta_3 - \frac{i\gamma_g}{2}) + i\rho_{34}(\Delta_4 + \frac{i\gamma_g}{2}), \\ \frac{\partial}{\partial t} \rho_{35} = -\frac{\Gamma}{2} \rho_{35} + \frac{i\Omega_{1,+1}^a}{2} \rho_{13}^* + \frac{i\Omega_{1,-1}^a}{2} \rho_{23}^* + \frac{i\Omega_{2,+1}^b}{2} \rho_{33} - \frac{i\Omega_{2,+1}^b}{2} \rho_{55} + \frac{i\Omega_{2,-1}^b}{2} \rho_{34} - i\rho_{35}(\Delta_3 - \frac{i\gamma_g}{2}), \\ \frac{\partial}{\partial t} \rho_{44} = \frac{\Gamma_2}{2} \rho_{55} + \frac{i\Omega_{2,-1}^b}{2} \rho_{45} - \frac{i\Omega_{2,-1}^b}{2} \rho_{45}^* + \frac{\gamma_g}{3} (\rho_{11} + \rho_{22} + \rho_{33}) - i\rho_{44}(\Delta_4 - \frac{i\gamma_g}{2}) + i\rho_{44}(\Delta_4 + \frac{i\gamma_g}{2}), \\ \frac{\partial}{\partial t} \rho_{45} = -\frac{\Gamma}{2} \rho_{45} + \frac{i\Omega_{1,+1}^a}{2} \rho_{14}^* + \frac{i\Omega_{1,-1}^a}{2} \rho_{24}^* + \frac{i\Omega_{2,+1}^b}{2} \rho_{34}^* + \frac{i\Omega_{2,-1}^b}{2} \rho_{44} - \frac{i\Omega_{2,-1}^b}{2} \rho_{55} - i\rho_{45}(\Delta_4 - \frac{i\gamma_g}{2}), \\ \frac{\partial}{\partial t} \rho_{55} = -\Gamma \rho_{55} - \frac{i\Omega_{1,+1}^a}{2} \rho_{15} + \frac{i\Omega_{1,+1}^a}{2} \rho_{15}^* - \frac{i\Omega_{1,-1}^a}{2} \rho_{25} + \frac{i\Omega_{1,-1}^a}{2} \rho_{25}^* - \frac{i\Omega_{2,+1}^b}{2} \rho_{35} \\ + \frac{i\Omega_{2,+1}^b}{2} \rho_{35}^* - \frac{i\Omega_{2,-1}^b}{2} \rho_{45} + \frac{i\Omega_{2,-1}^b}{2} \rho_{45}^*. \end{array} \right. \quad (S8)$$

As the direct population exchange rate between ground states is small, one may set ground states exchange rate $\gamma_g=0$. The decaying from excited states to the ground states $|F=1\rangle$ and $|F=2\rangle$ satisfy $\Gamma_1 : \Gamma_2 = 1 : 3$. In our experiment, the intensities of bichromatic light field are equal, so the four Rabi frequencies satisfy [S1, S3],

$$\Omega_{1,+1}^a : \Omega_{1,-1}^a : \Omega_{2,+1}^b : \Omega_{2,-1}^b = 1 : -1 : \sqrt{3} : \sqrt{3}. \quad (S9)$$

For simplicity, in theoretical analysis we do not consider degenerate Zeeman sublevels [S4], and set all four Rabi frequencies as the average Rabi frequency and the damping rates $\Gamma_1=\Gamma_2=\Gamma$. To compare with the experimental observation, the average Rabi frequency can be given as $\Omega = \sqrt{[(\Omega_{1,\pm 1}^a)^2 + (\Omega_{2,\pm 1}^b)^2] / 2}$ [S5]. Using the adiabatically eliminating (which implies consideration of the system at times $t \gg \frac{1}{\Gamma}$ and $\frac{\partial}{\partial t} \rho_{55} \approx 0$) [S6], solving Eq. S8, the excited state population can be given

$$\rho_{55} \approx \frac{\Omega}{\Gamma} (\text{Im}(\rho_{15}) + \text{Im}(\rho_{25}) + \text{Im}(\rho_{35}) + \text{Im}(\rho_{45})), \quad (S10)$$

which is relevant to the light absorption [S7]. For ^{87}Rb atoms, the excited-state decaying rate of D1 line is $\Gamma=2\pi \cdot 5.75$ MHz, and so that the accumulated excited-state population ρ_{55} is small comparing with that of ground states. Thus, in the near resonant region of $\delta \ll \Gamma$, we can simplify the time-evolution as

$$\left\{ \begin{array}{l} \frac{\partial}{\partial t} \rho_{15} \approx -\frac{\Gamma}{2} \rho_{15} + \frac{i\Omega}{2} \rho_{11} + \frac{i\Omega}{2} (\rho_{12} + \rho_{13} + \rho_{14}), \\ \frac{\partial}{\partial t} \rho_{25} \approx -\frac{\Gamma}{2} \rho_{25} + \frac{i\Omega}{2} \rho_{22} + \frac{i\Omega}{2} (\rho_{12}^* + \rho_{23} + \rho_{24}), \\ \frac{\partial}{\partial t} \rho_{35} \approx -\frac{\Gamma}{2} \rho_{35} + \frac{i\Omega}{2} \rho_{33} + \frac{i\Omega}{2} (\rho_{13}^* + \rho_{23}^* + \rho_{34}), \\ \frac{\partial}{\partial t} \rho_{45} \approx -\frac{\Gamma}{2} \rho_{45} + \frac{i\Omega}{2} \rho_{44} + \frac{i\Omega}{2} (\rho_{14}^* + \rho_{24}^* + \rho_{34}^*). \end{array} \right. \quad (S11)$$

Under adiabatically eliminating, solving Eq. S11, we can get

$$\begin{cases} \rho_{15} \approx \frac{i\Omega}{\Gamma} (\rho_{11} + \rho_{12} + \rho_{13} + \rho_{14}), \\ \rho_{25} \approx \frac{i\Omega}{\Gamma} (\rho_{22} + \rho_{12}^* + \rho_{23} + \rho_{24}), \\ \rho_{35} \approx \frac{i\Omega}{\Gamma} (\rho_{33} + \rho_{13}^* + \rho_{23}^* + \rho_{34}), \\ \rho_{45} \approx \frac{i\Omega}{\Gamma} (\rho_{44} + \rho_{14}^* + \rho_{24}^* + \rho_{34}^*). \end{cases} \quad (\text{S12})$$

The population of excited-state $\rho_{55} \ll 1$, then the population of ground state $\rho_{11} + \rho_{22} + \rho_{33} + \rho_{44} \approx 1$. Thus Eq. S10 reads

$$\begin{aligned} \rho_{55} &= \frac{\Omega^2}{\Gamma^2} (\rho_{11} + \rho_{22} + \rho_{33} + \rho_{44} + 2\text{Re}(\rho_{12}) + 2\text{Re}(\rho_{34}) \\ &\quad + 2\text{Re}(\rho_{13}) + 2\text{Re}(\rho_{24}) + 2\text{Re}(\rho_{14}) + 2\text{Re}(\rho_{23})) \\ &= \frac{\Omega^2}{\Gamma^2} (1 + 2\text{Re}(\rho_{12}) + 2\text{Re}(\rho_{34}) + 2\text{Re}(\rho_{13}) \\ &\quad + 2\text{Re}(\rho_{24}) + 2\text{Re}(\rho_{14}) + 2\text{Re}(\rho_{23})). \end{aligned} \quad (\text{S13})$$

This means that the excited-state population ρ_{55} is relevant to the real parts of six density-matrix elements $\{\rho_{12}, \rho_{34}, \rho_{13}, \rho_{24}, \rho_{14}, \rho_{23}\}$ [S6]. Combining Eq. S8 and Eq. S12, the time-evolution can be described by

$$\begin{cases} \frac{\partial}{\partial t} \rho_{12} = -\frac{\Omega^2}{4\Gamma} \left(\frac{1}{2} + 2\rho_{12} + \rho_{13} + \rho_{14} + \rho_{23}^* + \rho_{24}^* \right) - i\rho_{12}\Delta_{12}, \\ \frac{\partial}{\partial t} \rho_{34} = -\frac{\Omega^2}{4\Gamma} \left(\frac{1}{2} + 2\rho_{34} + \rho_{13}^* + \rho_{23}^* + \rho_{14} + \rho_{24} \right) - i\rho_{23}\Delta_{34}, \\ \frac{\partial}{\partial t} \rho_{13} = -\frac{\Omega^2}{4\Gamma} \left(\frac{1}{2} + 2\rho_{13} + \rho_{12} + \rho_{14} + \rho_{23} + \rho_{34}^* \right) - i\rho_{13}\Delta_{13}, \\ \frac{\partial}{\partial t} \rho_{24} = -\frac{\Omega^2}{4\Gamma} \left(\frac{1}{2} + 2\rho_{24} + \rho_{12}^* + \rho_{23} + \rho_{14} + \rho_{34} \right) - i\rho_{24}\Delta_{24}, \\ \frac{\partial}{\partial t} \rho_{14} = -\frac{\Omega^2}{4\Gamma} \left(\frac{1}{2} + 2\rho_{14} + \rho_{12} + \rho_{13} + \rho_{24} + \rho_{34} \right) - i\rho_{14}\Delta_{14}, \\ \frac{\partial}{\partial t} \rho_{23} = -\frac{\Omega^2}{4\Gamma} \left(\frac{1}{2} + 2\rho_{23} + \rho_{12}^* + \rho_{24} + \rho_{13} + \rho_{34}^* \right) - i\rho_{23}\Delta_{23}. \end{cases} \quad (\text{S14})$$

Where

$$\begin{cases} \Delta_{12} = \Delta_1 - \Delta_2 - i\gamma_{12}, \\ \Delta_{34} = \Delta_3 - \Delta_4 - i\gamma_{34}, \\ \Delta_{13} = \Delta_1 - \Delta_3 - i\gamma_{13}, \\ \Delta_{24} = \Delta_2 - \Delta_4 - i\gamma_{24}, \\ \Delta_{14} = \Delta_1 - \Delta_4 - i\gamma_{14}, \\ \Delta_{23} = \Delta_2 - \Delta_3 - i\gamma_{23}. \end{cases} \quad (\text{S15})$$

Subjected to bias magnetic field, the resonances of magneto-sensitive transitions are sufficiently separated in frequency to not overlap with the magneto-insensitive transitions, Eq. S14 can be further simplified as

$$\begin{cases} \frac{\partial}{\partial t} \rho_{12} \approx -\frac{\Omega^2}{2\Gamma} \left(\frac{1}{2} + 2\rho_{12} \right) - i\rho_{12}\Delta_{12}, \\ \frac{\partial}{\partial t} \rho_{34} \approx -\frac{\Omega^2}{2\Gamma} \left(\frac{1}{2} + 2\rho_{34} \right) - i\rho_{34}\Delta_{34}, \\ \frac{\partial}{\partial t} \rho_{13} \approx -\frac{\Omega^2}{2\Gamma} \left(\frac{1}{2} + 2\rho_{13} \right) - i\rho_{13}\Delta_{13}, \\ \frac{\partial}{\partial t} \rho_{24} \approx -\frac{\Omega^2}{2\Gamma} \left(\frac{1}{2} + 2\rho_{24} \right) - i\rho_{24}\Delta_{24}, \\ \frac{\partial}{\partial t} \rho_{14} \approx -\frac{\Omega^2}{2\Gamma} \left(\frac{1}{2} + 2\rho_{14} \right) - i\rho_{14}\Delta_{14}, \\ \frac{\partial}{\partial t} \rho_{23} \approx -\frac{\Omega^2}{2\Gamma} \left(\frac{1}{2} + 2\rho_{23} \right) - i\rho_{23}\Delta_{23}. \end{cases} \quad (\text{S16})$$

If Ω remains unchanged for a period of time, by solving Eq. S16, the solution of ρ_{14} is

$$\rho_{14}(t_0 + t) = f(\Delta_{14}) \left(1 - e^{-\left(i\Delta_{14} + \frac{\Omega^2}{\Gamma}\right)t} \right) + \rho_{14}(t_0) e^{-\left(i\Delta_{14} + \frac{\Omega^2}{\Gamma}\right)t} \quad (\text{S17})$$

with

$$f(x) = -\frac{\Omega^2}{4\Gamma \left(ix + \frac{\Omega^2}{\Gamma} \right)}, \quad (\text{S18})$$

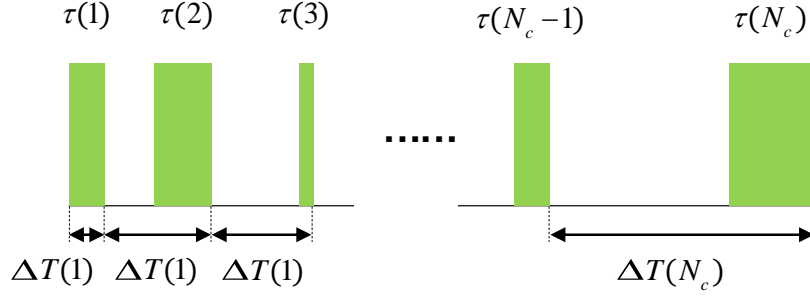


FIG. S6: **Time sequence of multi-pulses.** Each pulse length $\tau(k)$ and pulse interval $\Delta T(k)$ ($k \in \mathbb{N}$) are variable.

and t_0 is the initial time and t is the evolution time.

When a sequence of pulses is applied, ρ_{14} depends on the pulse length $\tau(k)$ and the pulse interval $\Delta T(k)$ as shown in Fig. S6. Given $\rho_{14}(0)=0$, according to Eq.S17, after the first pulse, we have

$$\begin{aligned} \rho_{14}^1 &= f(\Delta_{14}) \left(1 - e^{-\left(\frac{\Omega^2}{\Gamma} + i\Delta_{14}\right)\tau(1)} \right) \\ &= f(\Delta_{14}) \sum_{l=1}^1 e^{-\frac{\Omega^2}{\Gamma} \sum_{k=l+1}^1 \tau(k)} \left[1 - e^{-\left(\frac{\Omega^2}{\Gamma} + i\Delta_{14}\right)\tau(l)} \right] e^{-i\Delta_{14} \sum_{k=l+1}^1 \Delta T(k)}. \end{aligned} \quad (\text{S19})$$

Similarly, assume that after the N_t -th ($N_t \in \mathbb{N}$) pulse, we have

$$\rho_{14}^{N_t} = f(\Delta_{14}) \sum_{l=1}^{N_t} e^{-\frac{\Omega^2}{\Gamma} \sum_{k=l+1}^{N_t} \tau(k)} \left[1 - e^{-\left(\frac{\Omega^2}{\Gamma} + i\Delta_{14}\right)\tau(l)} \right] e^{-i\Delta_{14} \sum_{k=l+1}^{N_t} \Delta T(k)}. \quad (\text{S20})$$

Before applying the $(N_t + 1)$ -th pulse $\tau(N_t + 1)$, there is a time duration of $\Delta T(N_t + 1) - \tau(N_t + 1)$ without CPT light, thus we have

$$\begin{aligned} \rho_{14}^{N_t+1} &= f(\Delta_{14}) \left(1 - e^{-\left(\frac{\Omega^2}{\Gamma} + i\Delta_{14}\right)\tau(N_t+1)} \right) + \rho_{14}^{N_t} e^{-i\Delta_{14}(\Delta T(N_t+1) - \tau(N_t+1))} \times e^{-\left(\frac{\Omega^2}{\Gamma} + i\Delta_{14}\right)\tau(N_t+1)} \\ &= f(\Delta_{14}) \sum_{l=1}^{N_t+1} e^{-\frac{\Omega^2}{\Gamma} \sum_{k=l+1}^{N_t+1} \tau(k)} \left[1 - e^{-\left(\frac{\Omega^2}{\Gamma} + i\Delta_{14}\right)\tau(l)} \right] e^{-i\Delta_{14} \sum_{k=l+1}^{N_t+1} \Delta T(k)}. \end{aligned} \quad (\text{S21})$$

Note that if $l + 1 > N_t$, $\sum_{k=l+1}^{N_t} (\dots) = 0$. Then when N_c pulses are applied, we have

$$\rho_{14}(N_c \Delta T) = \sigma(\Delta_{14}), \quad (\text{S22})$$

where

$$\sigma(x) = f(x) \sum_{l=1}^{N_c} e^{-\frac{\Omega^2}{\Gamma} \sum_{k=l+1}^{N_c} \tau(k)} \left[1 - e^{-\left(\frac{\Omega^2}{\Gamma} + ix\right)\tau(l)} \right] e^{-ix \sum_{k=l+1}^{N_c} \Delta T(k)}. \quad (\text{S23})$$

Similar to the derivation of ρ_{14} , one can easily obtain

$$\rho_{ij}(N_c \Delta T) = \sigma(\Delta_{ij}) \quad (i, j \in \{1, 2, 3, 4\}, i \neq j). \quad (\text{S24})$$

Analog to the Fabry-Pérot cavity

According to Eq. S13 and Eq. S24, ρ_{55} can be expressed as

$$\begin{aligned} \rho_{55} &= \frac{\Omega^2}{\Gamma^2} \left\{ 1 + 2\text{Re}[\sigma(\Delta_{12})] + 2\text{Re}[\sigma(\Delta_{34})] + 2\text{Re}[\sigma(\Delta_{13})] \right. \\ &\quad \left. + 2\text{Re}[\sigma(\Delta_{24})] + 2\text{Re}[\sigma(\Delta_{14})] + 2\text{Re}[\sigma(\Delta_{23})] \right\}. \end{aligned} \quad (\text{S25})$$

Since the dephasing as well as the detuning near center resonance in magneto-sensitive coupling are large, so that $\{\rho_{12}, \rho_{34}, \rho_{13}, \rho_{24}\}$ can be neglected around $\delta=0$, that is,

$$\rho_{55} = \frac{\Omega^2}{\Gamma^2} \left\{ 1 + 2\text{Re}[\sigma(\Delta_{14})] + 2\text{Re}[\sigma(\Delta_{23})] \right\}. \quad (\text{S26})$$

Considering the weak magnetic field such that $|g_1 + g_2|\mu_B Bz/\hbar \ll \text{FWHM}$ (where FWHM is linewidth of conventional CPT spectrum) and $\gamma_{14}=\gamma_{23}=0$, we have

$$\Delta_{14} \approx \Delta_{23} \approx \delta. \quad (\text{S27})$$

Thus Eq. S26 can be further simplified as

$$\rho_{55} = \frac{\Omega^2}{\Gamma^2} \left\{ 1 + 4\text{Re}[\sigma(\delta)] \right\}. \quad (\text{S28})$$

Fixing the pulse length $\tau(k)=\tau$ and the pulse interval $\Delta T(k)=\Delta T$, according to Eq. S23, we have

$$\begin{aligned} \sigma(\delta) &= f(\delta) \sum_{l=1}^{N_c} e^{-\frac{\Omega^2}{\Gamma}(N_c-l)\tau} \left[1 - e^{-\left(\frac{\Omega^2}{\Gamma} + i\delta\right)\tau} \right] e^{-i\delta(N_c-l)\Delta T} \\ &= f(\delta) \sum_{l=1}^{N_c} \mathcal{R}^{(N_c-l)} \mathcal{T} e^{-i(N_c-l)\delta\Delta T} \\ &= f(\delta) \sum_{l=1}^{N_c} \mathcal{R}^{(l-1)} \mathcal{T} e^{-i(l-1)\delta\Delta T} \\ &= \sum_{l=1}^{N_c} \sigma_l(\delta), \end{aligned} \quad (\text{S29})$$

where $\sigma_l(\delta)=f(\delta)\mathcal{R}^{(l-1)}\mathcal{T}e^{-i(l-1)\delta\Delta T}$. Obviously, Eq. S29 is analogous to the transmission of light in a Fabry-

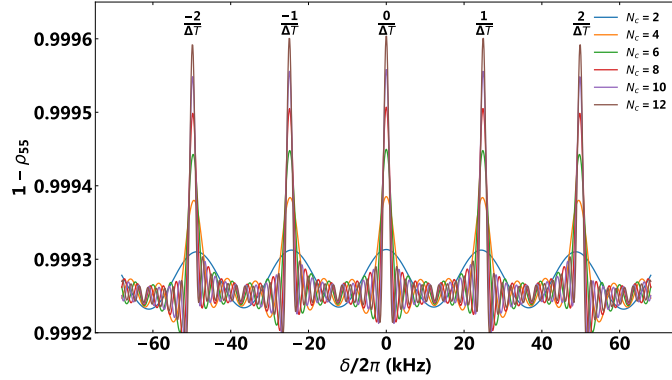


FIG. S7: **Analytical results of different pulse number N .** We set $\Omega=\frac{1}{2\pi}$ MHz, $\Delta T=0.04$ ms, $\tau=0.002$ ms. As N increases, the peaks become sharper at repeated frequency $\{\frac{n}{\Delta T} \mid n \in \mathbb{Z}\}$.

Pérot (FP) cavity. Here, the effective reflection coefficient $\mathcal{R} \equiv e^{-\frac{\Omega^2}{\Gamma}\tau}$, the effective transmission coefficient $\mathcal{T}=1 - e^{-\left(\frac{\Omega^2}{\Gamma} + i\delta\right)\tau}$ and the effective free spectral range (FSR) $\Delta\nu_{FSR}=\frac{1}{\Delta T}$. The constructive interference occurs when $\delta\Delta T=2m\pi$ ($m \in \mathbb{N}$), otherwise destructive interference occurs. In FIG. S7, we show the signals of $1 - \rho_{55}$ that are analogous to the transmission signal of FP cavity, where the constructive interference appears as comb-like resonant peaks at the frequencies: $\{\frac{n}{\Delta T} \mid n \in \mathbb{Z}\}$.

The above analyses are performed under the condition of $|g_1 + g_2|\mu_B B_z/\hbar \ll \text{FWHM}$ and so that the assumption of $\Delta_{14} \approx \Delta_{23} \approx \delta$ is valid. Actually, due to the small difference in two involved Landé g factors ($g_1 = -0.5017$ and $g_2 = 0.4997$), there is a frequency shift $2|g_1 + g_2|\mu_B B_z/\hbar = 5568 B_z$ Hz between the two transitions $\{|1\rangle \rightarrow |4\rangle, |2\rangle \rightarrow |3\rangle\}$ when a magnetic field B_z is applied. For a weak magnetic field, it only broadens the linewidth. But if the bias magnetic field is not too weak, the approximation $\Delta_{14} \approx \Delta_{23}$ becomes invalid, one has to use Eq. S26 instead of Eq. S28. Therefore the two-photon resonances occur at $\Delta_{14}=0$ or $\Delta_{23}=0$ and each peak splits into two new ones. In Fig. S8, we show that the analytical results (green line) are well consistent with the experimental signals (blue dash-dotted line). On one hand, we can eliminate the effects of Landé g factors on the clock transition frequency by averaging the frequencies of two peaks. On the other hand, the frequency difference between two peaks can be used to measure magnetic field without involving magneto-sensitive transitions.

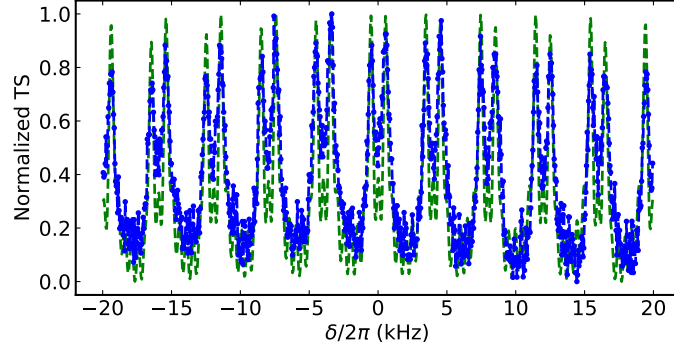


FIG. S8: **Multi-pulse CPT-Ramsey spectrum in presence of a non-weak bias magnetic field.** Each peak splits into two new ones. Green line is the analytical result of normalized $1 - \rho_{55}$, and blue dash-dotted line is the experimental data. The parameters are chosen as $\Omega = \frac{2.36}{2\pi}$ MHz, $\Delta T = 0.25$ ms, $\tau = 2$ μ s, $B_z = 0.2$ G and $N = 7$.

Numerical Simulation

Generally, one has to numerically solve the optical Bloch equation S8. And we set $\gamma_{12} = \gamma_{13} = \gamma_{24} = \gamma_{34} = \gamma_c$ for describing the dephasing induced by magnetic-field fluctuation. In our simulation, we assume the population exchange rate from each ground state $\gamma_g = 0$ and the Rabi frequencies are set according to Eq. S9.

According to Eq. S28, $(1 - \rho_{55})|_{\tau \rightarrow \infty} \sim A_1 f(\delta) + A_2$, where A_1 and A_2 are adjustable coefficients. When the magnetic field B_z is weak, the average Rabi frequency Ω can be obtained by fitting the central peak of experimental CPT spectrum using formula $A_1 f(\delta) + A_2$. Eq. S8 can be constructed as

$$\frac{\partial}{\partial t} \mathbf{V}(t) = \mathbf{M}(t) \mathbf{V}(t), \quad (\text{S30})$$

where \mathbf{M} is the time-dependent coefficient matrix, \mathbf{V} corresponds to the density matrix ρ being reshaped into one-dimensional vector. In a short time step t_1 , \mathbf{M} can be regarded as a constant matrix, thus we have

$$\mathbf{V}(t_0 + t_1) = \exp(\mathbf{M}t_1) \mathbf{V}(t_0). \quad (\text{S31})$$

Comparison between numerical and experimental results

In the experiment, the single-pulse CPT spectrum is collected by sampling and averaging the rear 285 μ s of the preparation pulse of CPT laser, as shown in Fig. S9. Fig. S10 shows the numerical result is consistent with experimental CPT spectrum.

The multi-pulse interference are implemented by inserting corresponding CPT pulses between CPT-Ramsey pulses respectively called as preparation and detection. Then one detection pulse starts to be emitted, and the length of the

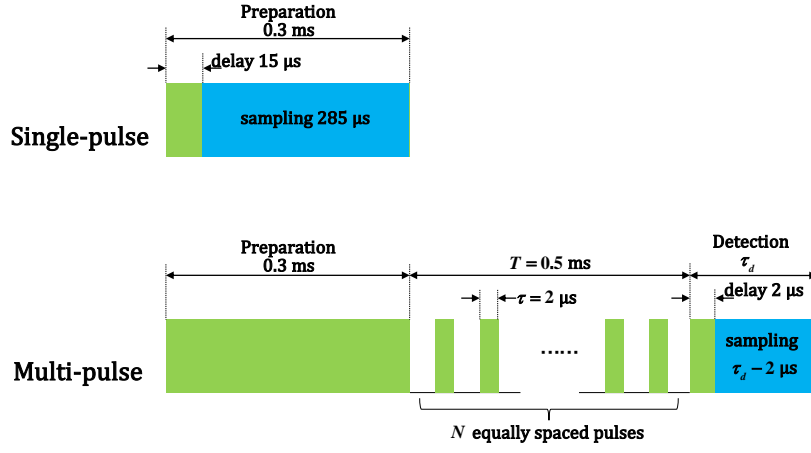


FIG. S9: **Timing sequence of single-pulse and multi-pulse CPT laser.** The preparation pulse is 0.3 ms, integration time $T=0.5$ ms and the time of detection pulse τ_d . For single-pulse CPT, the signal is collected by sampling and averaging the rear 285 μ s of preparation pulse. For multi-pulse interference, the equally spaced N pulses are implemented between preparation pulse and detection pulse. The pulse length $\tau=2\mu$ s and the total integration time $T=0.5$ ms. When the detection pulse starts to be emitted. After a delay of 2 μ s, the signal is obtained by sampling and averaging the remaining detection pulse. The sampling rate is 1 MHz.

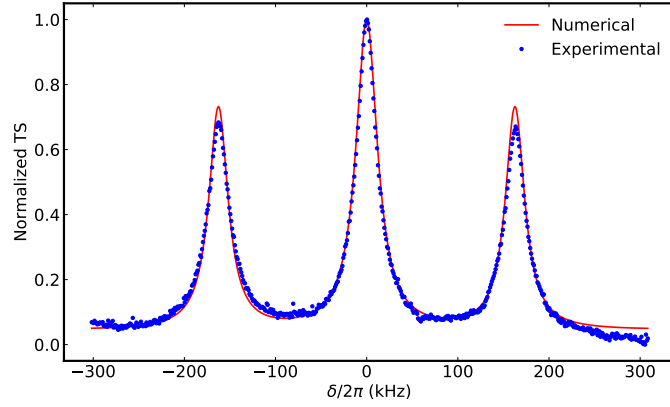


FIG. S10: **The normalized single-pulse CPT spectrum of experimental signal (blue dots) and the numerical result (red line) of the normalized $1 - \rho_{55}$.** The parameters used in numerical simulation are set as $\pm\Omega_{1,+1}^a = \frac{1}{\sqrt{3}}\Omega_{2,\pm 1}^b = \frac{1.25}{2\pi}$ MHz, $B_z=0.116$ G and $\gamma_c = \frac{0.012}{2\pi}$ MHz.

probe light is τ_d . The signal is obtained by sampling and averaging this pulse with 2 μ s delay. The sampling rate is 1 MHz of both single-pulse and multi-pulse spectrum.

To discuss the γ_c , we perform the multi-pulse experimental and numerical result. As the Fig. S11 shown, by comparing the experimental and numerical result, we find they agree better when setting $\gamma_c = \frac{0.012}{2\pi}$ MHz.

In order to obtain a better experimental signal, we generally set the detection pulse $\tau_d=8$ μ s and average this pulse after a delay of 2 μ s. However, near the $\delta=0$ the ρ_{13} and ρ_{24} can be considered to be rapidly oscillating. These items will be averaged out if the detection time is long. Therefore the detection pulse is set to $\tau_d=3$ μ s in order to observe the peaks of these terms.

Comparison between numerical and analytical results

Both numerical and analytical parameters are set as $\Omega_{1,\pm 1}^a = \Omega_{2,\pm 1}^b = \Omega = \frac{1.25}{2\pi}$ MHz, $\gamma_g=0$, $\gamma_{14}=\gamma_{23}=0$, $\Gamma_1=\Gamma_2=\frac{1}{2}\Gamma$, $\gamma_c = \frac{0.012}{2\pi}$ MHz and detection time $\tau_d=3$ μ s. The analytical result is referring to Eq. S25 and Eq. S26. Fig. S12 shows

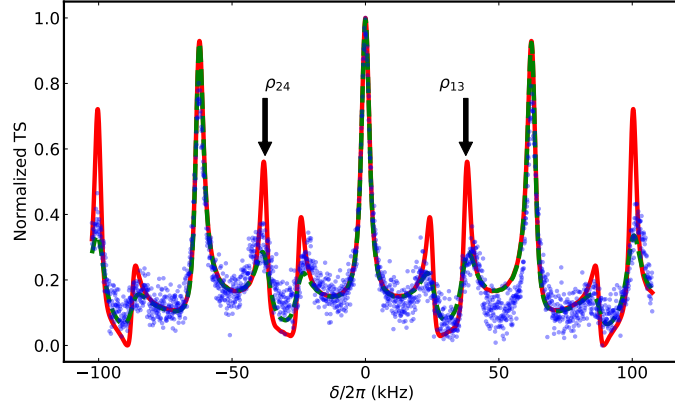


FIG. S11: Numerical result (green line for $\gamma_c=0$ and red line for $\gamma_c=\frac{1.2}{2\pi}$ MHz) and experiment (blue dots). The preparation time is 0.3 ms, total free-evolution time $T=0.5$ ms and 31 pulses with the length $\tau=2 \mu\text{s}$ is inserted. The length of detection pulse $\tau_d=3\mu\text{s}$. The parameters used in numerical simulation are set as $\pm\Omega_{1,+1}^a=\frac{1}{\sqrt{3}}\Omega_{2,\pm 1}^b=\frac{1.25}{2\pi}$ MHz, $B_z=0.116$ G. The constructive peaks of ρ_{13} and ρ_{24} are annotated.

that the numerical results agree with Eq. S25 as well as the Eq. S26, which means the neglect of ρ_{12} , ρ_{34} , ρ_{13} and ρ_{24} is feasible when γ_c is relatively large. However, there are some critical cases, in which $\{|g_1 - g_2|\mu_B/\hbar = m\frac{1}{\Delta T} \mid m \in \mathbb{N}\}$,

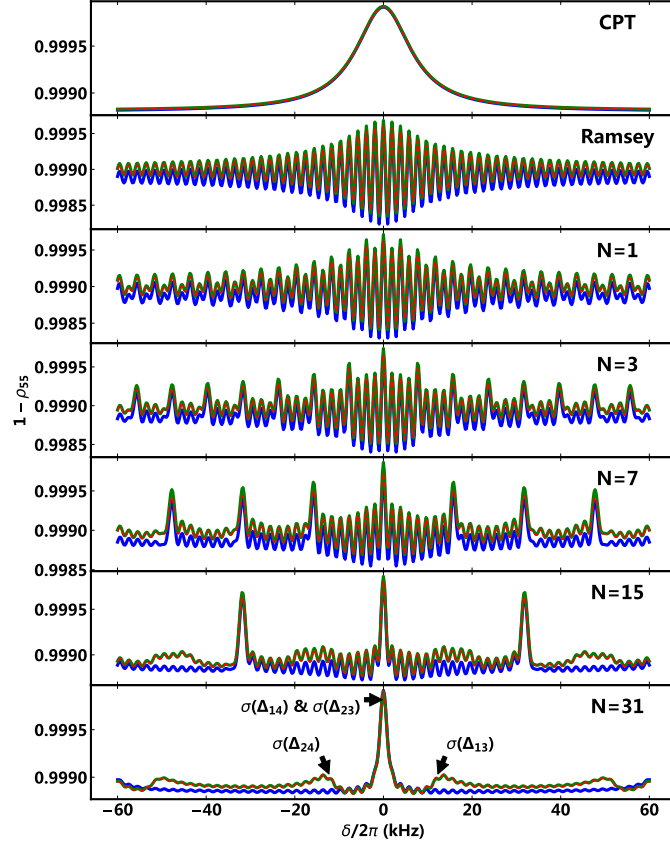


FIG. S12: Numerical (red dash) and analytical result (green line for Eq. S25 and blue line for Eq. S26). The preparation time is 0.3 ms, total free-evolution time $T=0.5$ ms and N pulses with the length $\tau=2 \mu\text{s}$ is inserted. Bias magnetic field is set as $B_z=0.1$ G. During detection pulse, the second sample of $1 - \rho_{55}$ is collected as the signal. In the last subplot with $N=31$, the peaks corresponding to the different components are annotated.

the constructive peaks of $\sigma(\Delta_{13})$ and $\sigma(\Delta_{24})$ will overlay with that of $\sigma(\Delta_{14})$ and $\sigma(\Delta_{23})$ at $\delta=0$. In this specific

situation, the approximation of Eq. S16 is not so precise that analytical result has a slight difference with simulated result (the 3rd subplot) in Fig. S13.

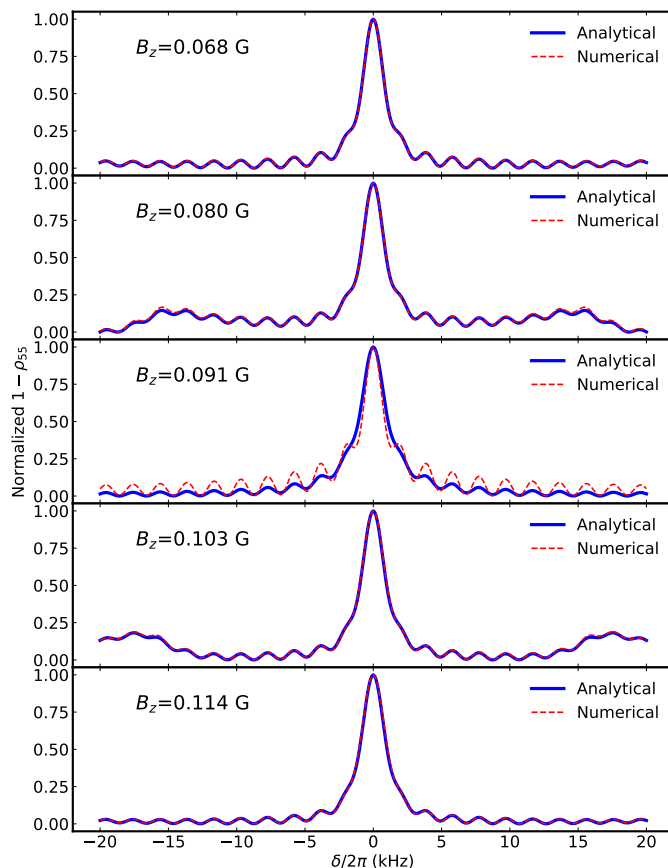


FIG. S13: Numerical (red dash) and analytical (blue line) signals in different B_z . The preparation time is 0.3 ms, total free-evolution time $T=0.5$ ms and 31 pulses with the length $2\ \mu\text{s}$ is inserted. During the detection, the second sample of $1 - \rho_{55}$ is collected as signal. When $B_z=0.091$ G, the analytical result has a little difference with numerical result.

* Electronic address: hjiahao@mail2.sysu.edu.cn

† Electronic address: lubo3@mail.sysu.edu.cn

‡ Electronic address: lichaoh2@mail.sysu.edu.cn

- [S1] M.S. Shahriar, Ye Wang, Subramanian Krishnamurthy, Y. Tu, G.S. Pati, and S. Tseng, “Evolution of an N-level system via automated vectorization of the liouville equations and application to optically controlled polarization rotation,” *J. Mod. Opt.* **61**, 351–367 (2014).
- [S2] I. Baumgart, J.-M. Cai, A. Retzker, M.B. Plenio, and Ch. Wunderlich, “Ultrasensitive magnetometer using a single atom,” *Phys. Rev. Lett.* **116**, 240801 (2016).
- [S3] Daniel A Steck, “Rubidium 87 d line data,” (2001).
- [S4] Ying-Cheng Chen, Chung-Wei Lin, and Ite A. Yu, “Roles of degenerate zeeman levels in electromagnetically induced transparency,” *Phys. Rev. A* **61**, 053805 (2000).
- [S5] P. R. Hemmer, M. S. Shahriar, V. D. Natoli, and S. Ezekiel, “Ac stark shifts in a two-zone Raman interaction,” *J. Opt. Soc. Am. B* **6**, 1519–1528 (1989).
- [S6] D. S. Chuchelov, E. A. Tsygankov, S. A. Zibrov, M. I. Vaskovskaya, V. V. Vassiliev, A. S. Zibrov, V. I. Yudin, A. V. Taichenachev, and V. L. Velichansky, “Central ramsey fringe identification by means of an auxiliary optical field,” *J. Appl. Phys.* **126**, 054503 (2019).
- [S7] E. Breschi, G. Kazakov, R. Lammegger, G. Miletì, B. Matisov, and L. Windholz, “Quantitative study of the destructive quantum-interference effect on coherent population trapping,” *Phys. Rev. A* **79**, 063837 (2009).